Short- and long-term observations of fracture permeability in granite by flow-through tests and a comparative observation by X-ray CT

Chenlu Song[1], Shinchiro Nakashima[2], Ryunosuke Kido[3], Hideaki Yasuhara[4] and Kiyoshi Kishida[1]

[1,5] Department of Urban Management, Kyoto University, Kyoto, 615-8540, JAPAN.

[2] Department of Civil and Environmental Engineering, Yamaguchi University, Yamaguchi, 755-8611 JAPAN

[3] Department of Civil and Earth Resources Engineering, Kyoto University, Kyoto, 615-8540, JAPAN.

[4] Department of Civil and Environmental Engineering, Ehime University, Matsuyama, 790-8577, JAPAN.

Abstract

To grasp the fracture contact-area variation is a kernel on understanding the permeability evolution of the fractured rocks. However, there is a lack of studies focusing on measuring the long-term fracture contact-area variation under different conditions. In this study, a series of short- and long-term permeability tests under coupled conditions are performed to check the permeability performance. Permeability is sensitive to confining pressures and shows temperature dependence in the short-term tests, and it has the irreversible change and time-dependence in the long-term tests. In order to verify the permeability evolution, by assembling a triaxial cell with heating capability, a microfocus X-ray CT is developed to observe the internal fracture structure change under the same conditions with the long-term permeability tests. The fracture aperture and the fracture contact-area ratio are calculated by CT image analysis technique. The estimated aperture decreases with increase of the confining pressure, and it decreases with time under the constant confining pressure. Moreover, the hydraulic aperture calculated from the CT observation is qualitatively consistent with that measured in the long-term permeability tests. It is clarified that the fracture contact-area increase with time under the constant confining pressure corresponds to the permeability decrease in the long-term.

Keywords: Permeability, short- and long-term, X-ray CT observation, contact-area ratio and aperture distribution

Introduction

The flow behavior in the deep subsurface has been given great attention in recent years. The coupled thermal-hydraulic-mechanical-chemical (THMC) processes exert a significant effect on the subsurface fluid flow in geological systems (Ghassemi et al., 2007; Taron et al., 2010; Frdric et al., 2017). Especially during the geological disposal of high-level radioactive waste, the stability of the disposal system may be affected by the long-term water flow around the rock fractures (Rutqvist et al., 2002; Yasuhara et al., 2015; Tsang et al., 2012;). Moreover, the coupled THMC processes might change the underground water flow paths, and then the transport of radionuclides will be promoted. Under the coupled interaction, the mechanical creep (stress corrosion) (Yasuhara et al., 2006; Xu et al., 2016) and the geochemical response (variation in mineral composition) (Polak and Beeler, 2004; Yasuhara et al., 2006, 2011; Elkhoury et al., 2013) altering the fracture surface roughness and transforming the long-term permeability evolution are discussed.

Several numerical works focusing on the prediction of the variation in permeability under the coupled THMC processes have been proposed (Taron et al., 2010; Zhang et al., 2013; Wang, 2017). However, not many laboratory works have addressed the long-term fluid flow behavior within the rock fractures or the changing of the fracture contact-area under the THMC coupled processes (Li et al., 2008; Yasuhara et al., 2015; Xu et al., 2016). Polak et al. (2003), Yasuhara et al. (2015), and Farough et al. (2016) conducted several long-term experiments, and the results showed that the fracture surface roughness was altered, and the aperture decreased at higher temperatures, which resulted in the permeability reduction. From the experimental studies, it is seen that under the coupled processes, the fracture contact-area should be evolved with time.

Subsequently, the fluid flowing through the fracture would be disturbed by the evolved fracture contact-area (Zimmerman et al., 1996; Li et al., 2008; Kishida et al., 2013). However, the evolution of the fracture contact-area has not been well investigated in the previous studies, because it is not simple to grasp the fracture contact-area immediately through the laboratory tests.

From the previous works, it is noted that the temporal fracture structure change needs to be further investigated. X-ray computed tomography (CT) (Van et al., 2001; Yao et al., 2009; Ketcham et al., 2010) is an effective technique which can~~is capable of~~ detecting the internal structure non-destructively and three-dimensionally (Robert et al., 1993; Fan et al., 2018). Therefore, it is possible to grasp various rock samples with fractures or cracks under the flow test. (Stephanie et al., 2001; Karpyn et al., 2007, 2009; Dustin et al., 2017; Lu and Kumaria, 2018). The measured data is used to reconstruct a 3D view for illustrating the fracture heterogeneous distribution (Keller, 1998; Kawakata et al., 1999; Mazumder et al., 2006; Yao et al., 2009; Richard et al., 2010; Hamed et al., 2016). Moreover, some researchers try to use microfocus X-ray CT to observe the fracture changing under varying conditions (Polak et al., 2003; Yasuhara et al., 2015; Okamoto et al., 2017). Polak et al., (2003) studied the fracture change under different temperatures (20, 80 and 120 °C), the mass removed from the fracture contact-area and the decrease in hydraulic aperture were investigated. Okamoto et al., (2017) showed a comparison of the CT scanning images between a sample at room temperature and at the temperature of 350°C. The quartz distribution illustrated that the flow rate was changed due to the mineral dissolution or the precipitation generated at 350°C. Yasuhara et al., (2015) conducted a series of permeability tests with several types of rock samples. Pore structures were observed through X-ray CT with a comparison between the pre- and post-experiment. The changing pore structures might support the variation in permeability. (Caulk et al., 2016; Kamali-Asl et al., 2018) found that the aperture would close at higher levels of confining stress. The higher levels of confining stress resulted in a change in the sensitivity of the variable fracture contact-area ratio.

However, previous laboratory studies have not directly observed the temporal change of the fracture contact-area under the coupled conditions. There is a lack of interpretation of the relationship between the long-term permeability changing and the fracture contact-area variation through laboratory works. Therefore, to further understand the long-term permeability evolution under coupled processes, this study focuses on several permeability tests under different conditions, especially for the variation in permeability over the long-term under a constant confining pressure. An X-ray CT observation as well as the long-term permeability tests are conducted to obtain the changes of the aperture distribution and the fracture contact-area. Finally, several indexes, such as the fracture contact-area ratio, the aperture distribution and a comparison of the hydraulic aperture change, are discussed.

2. Sample materials and experimental procedures

2.1 Fracture generation and morphology

Figure 1 presents the geometry of the samples used in this study. Two cylindrical granite samples, Sample #1 and Sample #2, with a size of 49.3×101.2 mm and 15.2×33.3 mm, respectively, are employed. Samples #1 and #2 are used for the permeability tests and the X-ray CT observation, respectively. Before the experiments, both samples are split by the Brazilian tensile testing method to create a single fracture along the cylinder axis (Fairhurst, 1964). The mechanical properties of the granite samples are listed in **Table 1**.

Table 1 Mechanical properties of granite sample

Sample	Uniaxial compression strength (MPa)	Young's modulus (GPa)	Poisson's ratio	Tensile strength (MPa)
Granite	140.3	55.4	0.2	6.2

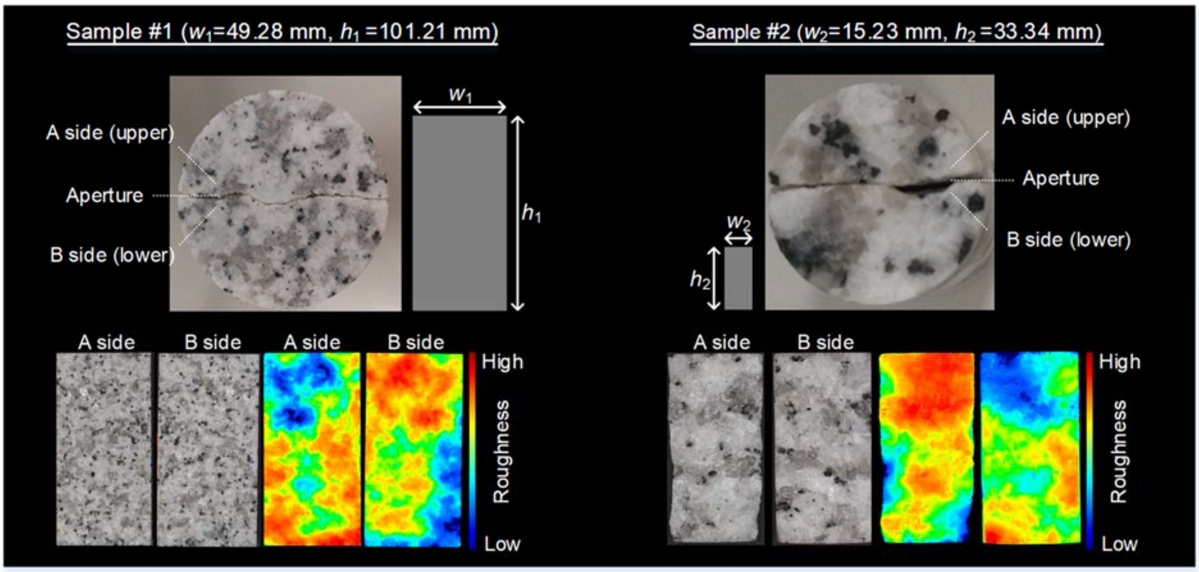

Fig. 1 Sample experiments and fracture surfaces measured by laser profilometer

In this study, the initial granite surface roughness before the experiments is evaluated by the JRC values. An optical profilometer is employed, using the pattern projection method (VR-3200, Keyence Corporation in Japan), to grasp the morphology of the fracture surfaces. The profilometer is capable of measuring the surface roughness in a grid pattern through non-contact. The grid size of the elevation measurement is 25 μm and the measurement resolution of the profilometer is 0.1 μm. The color contour maps in **Fig. 1** illustrate the elevations of the surface roughness.

To clarify the variation in fracture surface roughness, it is necessary to grasp the surface roughness precisely before starting the experiments. Barton's standard of JRC (Joint Roughness

Coefficient) profiles is selected as the comparison index. Typically, the JRC value ranges from 0 to 20 in the shear behavior of the rock joints (Barton et al., 1977,1997). The JRC values can be calculated with the dimensionless parameter Z_2 (Tse ta al., 1979), which has been widely discussed and is defined as follows (Zhang and Dimadis, 2014; Yin et al., 2017; Yong et al., 2018):

$$Z_2 = \left[\frac{1}{M-1}\sum_{i=1}^{M-1}\left(\frac{\Delta y}{\Delta x}\right)_1^2\right]^{\frac{1}{2}} \quad (1)$$

where Δx is the sampling interval, Δy is the difference between two adjacent points and M is the number of sampling points along the length of the fracture surface. Subsequently, the JRC values can be evaluated by

$$JRC = 60.32Z_2 - 4.51(\Delta x = 0.25\ mm) \quad (2)$$

Table 2 lists the Z_2 and JRC values for both surfaces of Samples #1 and #2. The JRC values for the two samples are around 20. The initial values are used to evaluate the difference in surface roughness between the pre- and post-experiment.

Table 2 Comparison of Z2 and JRC values with profilometer equipment (VR-3200)

	(JRC=60.32* Z_2-4.51) 0.25 mm	
	A side	B side
Sample #1	19.9	20.2
Sample #2	22.8	20.4

2.2 Transient pulse method

To investigate the permeability evolution under various conditions, the transient pulse method is applied to measure the permeability value (Hsieh et al., 1981). The pore water pressures between the upstream and downstream in Eq. (3) are different. The tank is located upstream of the sample. The pressure is increased by the operator in tiny increments of the injected water, then the permeability is measured from the pressure gradient generated between the two ends of the sample and the lapse of time. With the passage of time, the difference in pressure will reach a new equilibrium, given as:

$$P_d = \frac{V_u P_u^0 + V_d P_d^0}{V_u + V_d} - \frac{V_u}{V_u + V_d}(P_u^0 - P_d^0)\exp\left(-\frac{k}{\beta\mu}\frac{A}{L}\frac{V_u + V_d}{V_u V_d}t\right)$$

$$P_u = \frac{V_u P_u^0 + V_d P_d^0}{V_u + V_d} - \frac{V_d}{V_u + V_d}(P_u^0 - P_d^0)\exp\left(-\frac{k}{\beta\mu}\frac{A}{L}\frac{V_u + V_d}{V_u V_d}t\right) \quad (3)$$

Where P_u and P_d are the upstream and downstream pressure, respectively, and V_u and V_d are the volume of two reservoirs, i.e., the volume of each reservoir is equal to 0.001 m^3 in this work. *A* and *L* are the cross-section and the length of the sample, respectively, μ is the viscosity of the fluid and β is the fluid compressibility. μ and β are temperature-dependent (Walsh, 1981). Then the coefficient of permeability can be evaluated from the following equations:

$$\ln\left((P_u - P_d)/2\right) = \ln\left(\frac{V_d}{V_u + V_d}(P_u^0 - P_d^0)\right) - \frac{k}{\beta\mu}\frac{A}{L}\frac{V_u + V_d}{V_u V_d}t \quad (4)$$

$$\alpha = -\frac{k}{\beta\mu}\frac{A}{L}\frac{V_u + V_d}{V_u V_d} \quad (5)$$

In Eq. (5), *A* represents the cross-sectional area of the sample. In this study, however, the fluid only flows through the fracture aperture. Therefore, cross-section *A* should be changed to $A = b \times W$, where *W* is the width of the sample and *b* is the hydraulic aperture. Consequently, based on the cubic law, Eq. (5) is rewritten as follows:

$$\alpha = -\frac{b^3}{12\beta\mu}\frac{W}{L}\frac{V_u + V_d}{V_u V_d} \quad (6)$$

Figure 2 shows a schematic illustration of the test apparatus. The granite sample (Sample #1) is installed in a triaxial cell. The maximum pressure and temperature that can be prescribed are 20.0 MPa and 200ºC, respectively. The sample is sealed with a heat-shrinkable tube and fixed to pedestals inside the vessel. A thermocouple is installed to measure the temperature close to the sample. Two water storage tanks supply water that passes through Sample #1.

Differential pore water pressure gauges are used to measure the difference in pressure between the upstream and the downstream. To check the internal fracture effluent after each permeability test, distilled water is used as the injection fluid in this experiment.

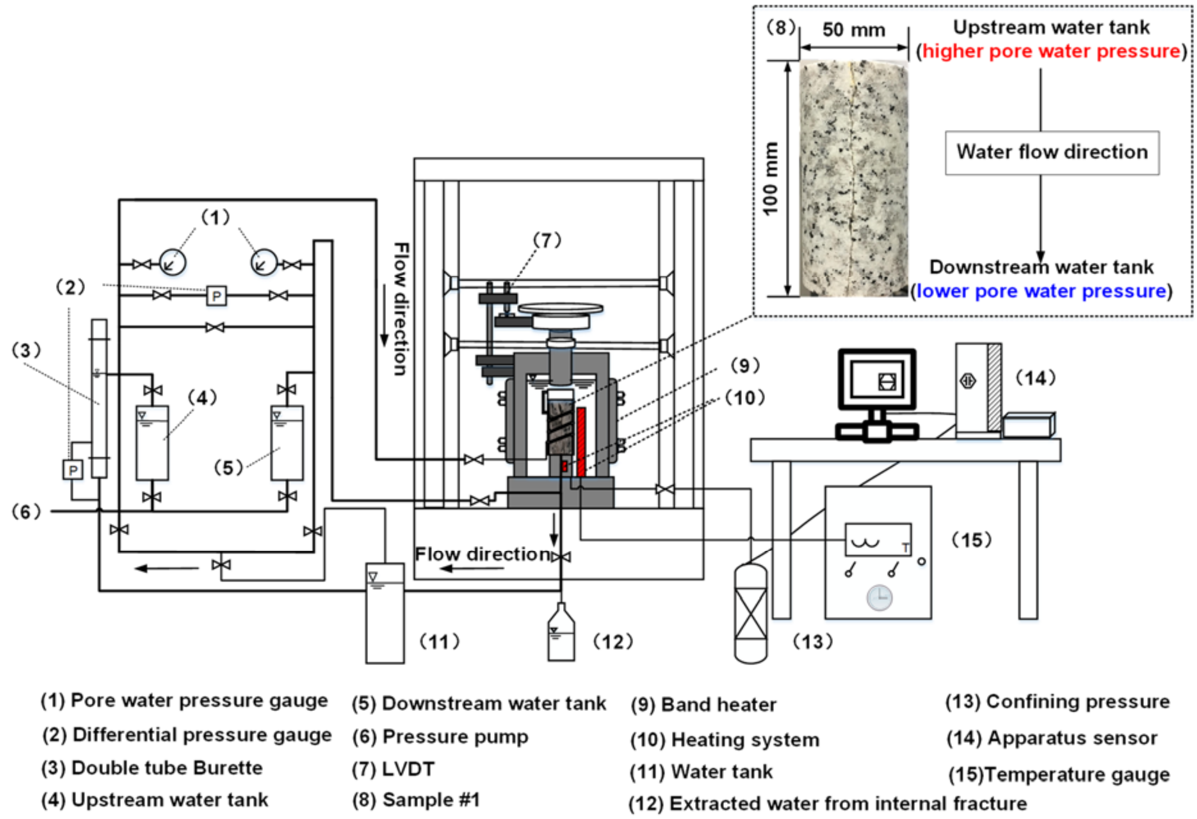

Fig. 2 Triaxial apparatus and Sample #1 installed in internal cell. The upstream and downstream pore water pressures are prescribed to the top and bottom of Sample #1, respectively

2.3 Experimental procedure of the permeability tests (Sample #1)

Figure 3 shows the experimental procedure of permeability tests. A series of permeability tests is conducted over both short- and long terms to observe the temporal changes in permeability. Short-term permeability tests are performed for 6 days, while long-term tests are performed for 180 days after the short-term tests finished. The short-term tests are carried out at three different temperatures of 20, 60, and 90 ºC. Three cycles of the loading-to-unloading process under each confining pressure are conducted. The confining pressure is increased in increments of 0.5 MPa from 1.0 to 3.0 MPa. The permeability tests are performed simultaneously at each confining pressure.

After the short-term tests, the temperature is decreased to 20 ºC. Then the long-term test is conducted under the confining pressure of 1.0 MPa and the temperature of 20 ºC. The confining pressure is increased from 1.0 to 3.0 MPa again and then keeps constant at 3.0 MPa for 180 days. During this process, the permeability is measured at the prescribed time intervals, as shown in **Fig. 3**. Simultaneously, the effluent is obtained from the internal fracture, to measure the element concentrations after each permeability test. The differential pore water pressures, fluid viscosity, and fluid compressibility are listed in **Table 3**. The permeability values are measured under various confining pressure conditions during the loading-to-unloading processes. **Fig.4** shows an example of the permeability tests. A difference in pressure between the upper and lower ends of the granite Sample #1 is produced with a slight change in the pore water pressures. Then, the permeability can be measured by the temporal change in the pressure difference during the elapsed time (600 seconds).

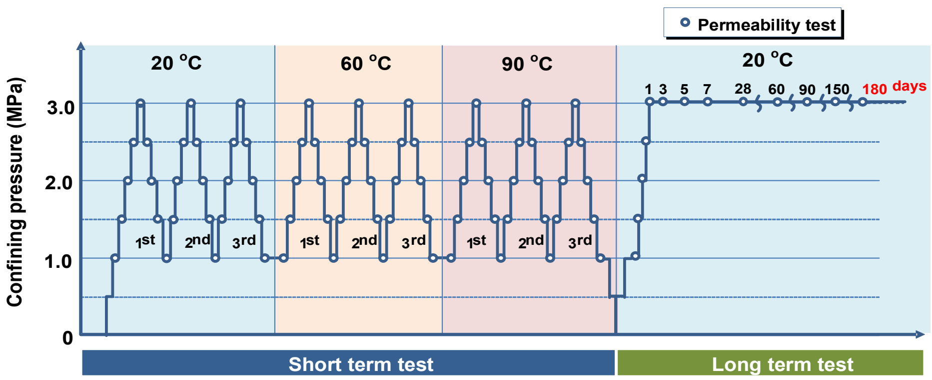

Fig. 3 Experimental procedure for short- and long-term permeability tests

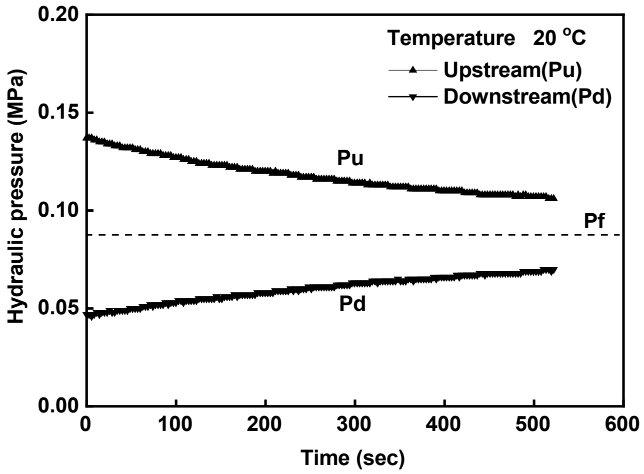

Fig. 4 Temporal changes in upstream and downstream water pressures in transient pulse tests

2.4 Non-destructive observation of fracture with microfocus X-ray CT (Sample #2)

In this study, a small-scale triaxial cell coupled with the X-ray CT equipment is developed to observe the change of the fracture structure in the rock under various confining pressures and temperatures, as shown in **Fig.5**. A lucid acrylic cell, without steel pillars, is utilized to make the cell as transparent to the X-ray as possible in order to avoid the X-ray attenuation by the steel (Otani et al., 2002). With a heater installed in the cell, the maximum confining pressure and temperature can be applied up to 3 MPa and 120 ºC, respectively. The X-ray CT equipment is KYOTO-GEOμXCT (TOSCANER-32250μhdk) (Kido et al., 2020). The minimum focus size is 4 μm and the resolution performance is 5 μm.

Figure 6 shows the CT slices scanned by the X-ray CT. A CT slice is composed of a number of voxels which include CT values determined based on the amount of the X-ray attenuation, depending on the material density. In the CT slice, white and black portions correspond to higher and lower density materials, respectively. The internal fracture structure of Sample #2 can be visualized in 3D by cumulating the CT slices obtained at each height of the sample.

Table 3 Experimental conditions of permeability tests

Confining pressure (MPa)	1.0	1.5	2.0	2.5	3.0
Pressure at upstream tank (MPa)	0.200	0.250	0.300	0.350	0.400
Pressure at downstream tank (MPa)	0.150	0.175	0.200	0.225	0.250
Fluid viscosity (10^{-10} Pas)	1.0017 (T=20 °C)		0.467 (T=60 °C)	0.0328 (T=90 °C)	
Compressibility (10^{-3} Pa)	4.5883 (T=20 °C)		4.3 (T=60 °C)	4.6 (T=90 °C)	

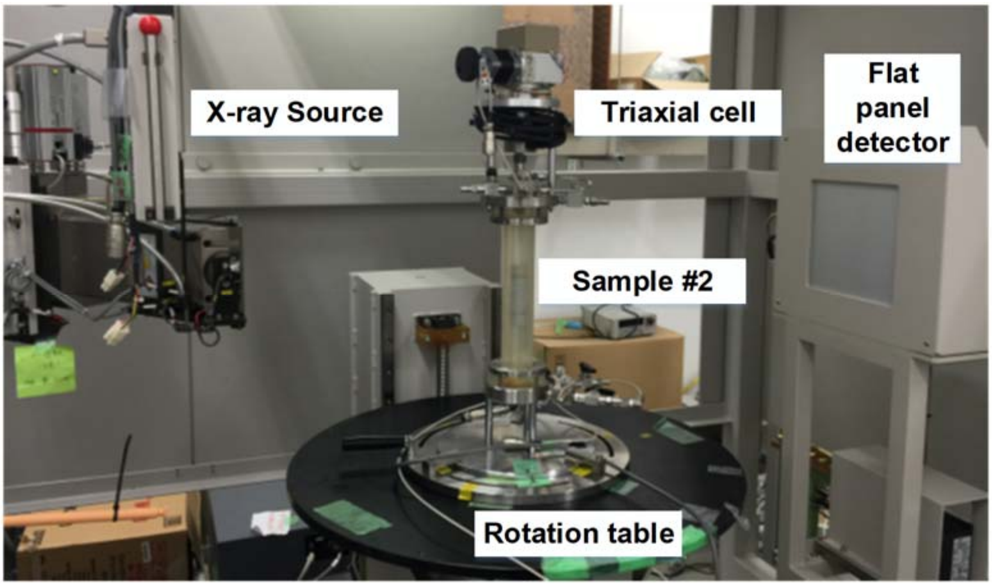

Fig. 5 Triaxial cell coupled with the microfocus X-ray CT equipment

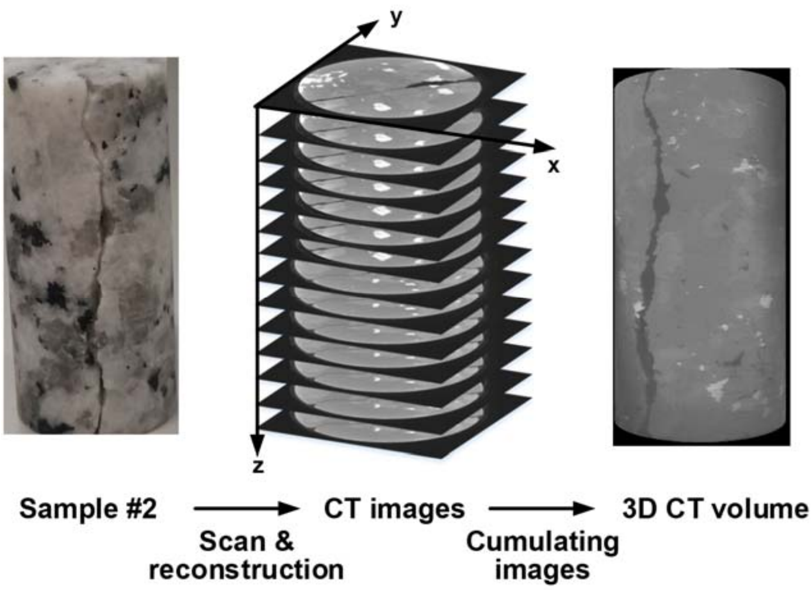

Fig. 6 3D CT volume of Sample #2

The scanning procedure for Sample #2 is as follows. Firstly, the initial fracture aperture is scanned at the as-received (dry) condition of 0 MPa and 20 ºC. Secondly, the sample is fixed in the triaxial cell under the water-saturated condition. The confining pressure is increased up to 3.0 MPa and the fracture aperture is scanned. These two scans are performed in one day. Subsequently, the confining pressure is kept constant at 3.0 MPa, and CT scans are performed at 14th, 30th, 60th, 90th, 120th, 150th and 180th days, corresponding to the same procedure with the permeability test of Sample #1. One CT slice comprises 1024 voxels in each *x*- and *y*-direction as shown in **Fig. 6**. At 0 MPa, the voxel size is 15.1 μm, 15.1 μm and 17.0 μm in *x*-, *y*- and *z*-directions. At 3.0 MPa, the voxel size is 18.4 μm, 18.4 μm and 21.0 μm, respectively.

2.5 Methodologies of CT image analysis

2.5.1 Segmentation

In order to detect the fracture aperture position in the CT volume scanning Sample #2, the segmentation of the CT images is required. As mentioned above, a CT slice is an assembly of discrete voxels including representative CT values for each material and thus, the segmentation can be performed based on the CT values. In the present study, the rock phase and the void phase in the CT images are distinguished from each other using a region growing method (Rosenfeld et al., 1982), which is implemented with the 3D image analysis software VGstudioMax3.1 (Volume Graphics GmbH) (Higo et al., 2014). This method examines the CT values of the neighboring voxels of initial seed voxels and determines whether the voxel neighbors should be added into the region of the seed groups. The regions are extended from the seed voxels to adjacent voxels depending on a region membership criterion, i.e., tolerance. The essential factors in the region growing method are initial seed voxel selection (3D location and CT value), a tolerance selection (range in CT values), and voxel connectivity for examination.

Figure 7 shows the outline of the image processing in this study. The procedure of the segmentation using the region growing method is as follows:

1) Assuming that a histogram of CT values for a homogeneous material follows a normal distribution, a mean CT value of the rock phase, μ_{ρ}, is obtained by analyzing the CT values using the VGstudioMax3.1. In this study, the mean rock CT value of 151 is chosen as the initial seed of the rock phase.
2) Similarly, the mean CT value of the void phase, μ_{ϖ}, of 48 is obtained. A threshold between the rock phase and the void phase is an intersection of the CT value histogram (see in **Fig. 7(a)**). In this study, the threshold value is 82.
3) The tolerance of the rock phase, T, is the difference between the mean CT value of the rock phase and the threshold determined in the above step, i.e., the tolerance is 69. Adjacent voxels to the initial seed voxel whose CT values are from μ_{ρ}-T to μ_{ρ}+T (i.e., from 82 to 220) are assimilated into the rock phase seed groups. The voxel connectivity of the region growing is a 26-connected neighborhood in 3-dimensional, which ensures the continuity of adjacent voxels to the initial seed voxel in *x*-, *y*- and *z*-directions (see **Fig. 7(b)**).
4) This process is iterated on until all of the neighboring voxels of the rock phase are assimilated and no further significant change is found. The remaining voxels after the iterative process of the region growing for the rock phase are regarded as the void phase, a segmentation CT image for the rock and void phase is depicted in **Fig. 7(c)**.

2.5.2 Detection of fracture aperture and calculation of fracture contact-area

Figure 7(d) shows the detection method of the internal aperture position from a CT segmentation image. A rectangular area, 800 voxels in *x*-direction and 360 voxels in *y*-direction is extracted from the segmentation image as an analysis region where the whole aperture part exists. At first, an exploration window, 1 voxel in *x*-direction and 360 voxels in *y*-direction is defined. Second, each voxel in the exploration window is searched in the *y*-direction. Then, the position where a voxel of the rock phase locates above a voxel of the void phase is detected as the upper aperture, whereas the position where a voxel of the rock phase locates below a voxel of the void phase is detected as the lower aperture. As shown in **Fig. 7(d)**, the aperture width corresponds to the number of voxels for the void phase between the upper and lower apertures. If there is no voxel for the void phase in the exploration window, this position is regarded as the fracture contact-area. The voxel search is performed for the exploration window set at each *x*-coordinate in the analysis region. In this study, the number of contact-area positions to the number of voxels in the *x*-direction of the analysis region is defined as the fracture contact-area ratio.

The same processing as mentioned above is applied to all of the segmentation images, providing the internal fracture information, i.e., aperture distribution and the fracture contact-area ratio of Sample #2.

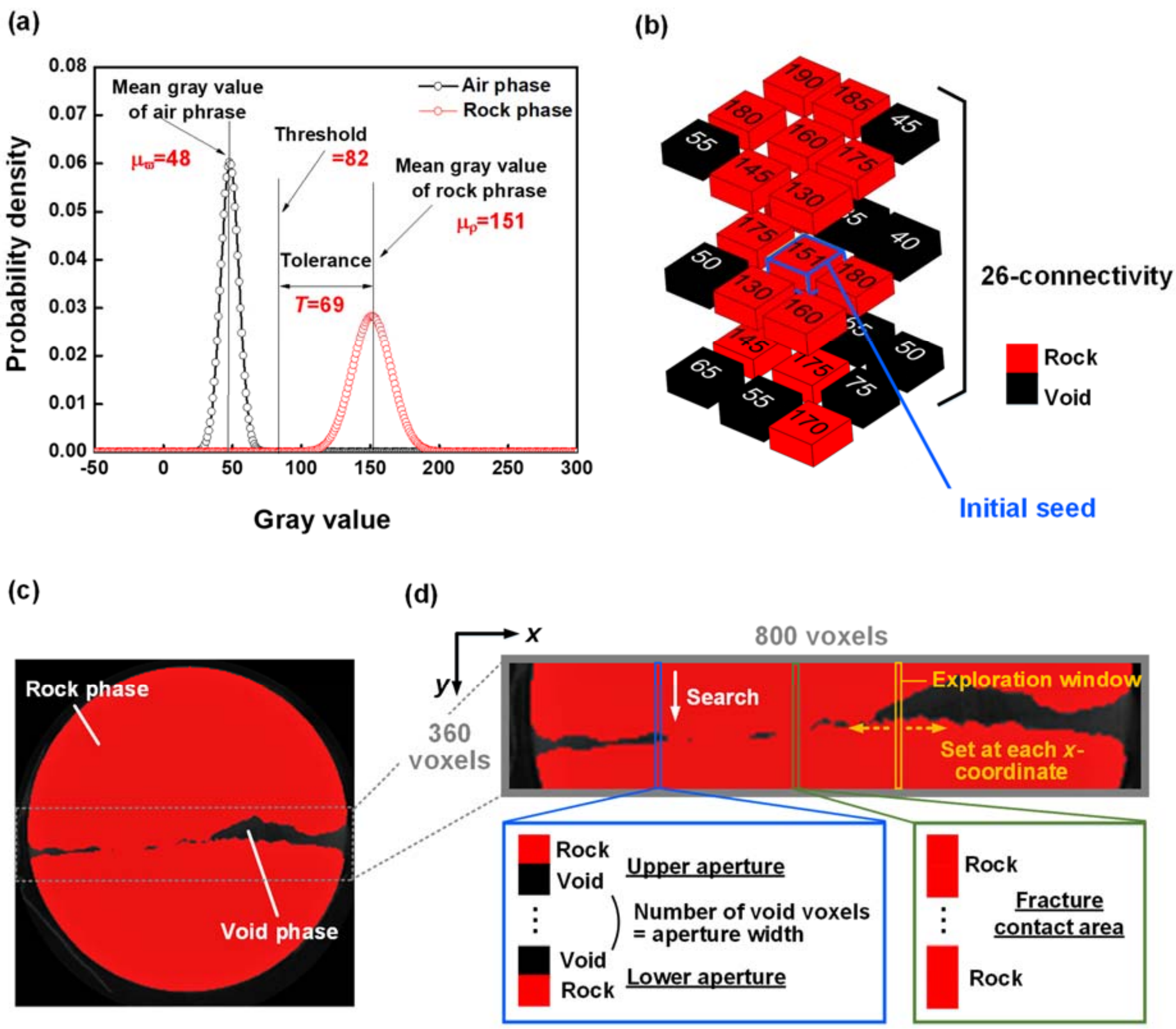

Fig. 7 Segmentation process for rock phase and void phase by region-growing technique:(a) determination of region growing, (b) schematic illustration of region growing in 3D, voxel connectivity of 26-connected neighborhood (c) segmentation image in 2 dimensional and (d) voxel that includes rock and void phases (aperture detection method) and fracture contact-area in aperture position

2.5.3 Validation of the CT image analysis

Figures 8(a) and **(b)** present the contour map of the surface roughness (Sample #2) measured by the optical profilometer (VG-3200) and that are analyzed by the CT image analysis method. For both of them the data are obtained at 0 MPa, as-received condition before starting the experiment. It is clarified that the extracted surface roughness of Sample #2 under the two methods is qualitatively similar to each other. **Figure 8(c)** shows the contour map of the aperture distribution measured by the CT image analysis. This distribution is derived from the aperture width for each CT slice, i.e., the difference between the upper aperture and the lower aperture, as mentioned in Subsection 2.5.2. The blue part of the contour map in **Fig. 8(c)** represents the fracture contact-area. The initial arithmetical mean aperture (hereinafter called the mechanical aperture) and the fracture contact-area ratio without the confining pressure are 0.253 mm and 5.4%, respectively.

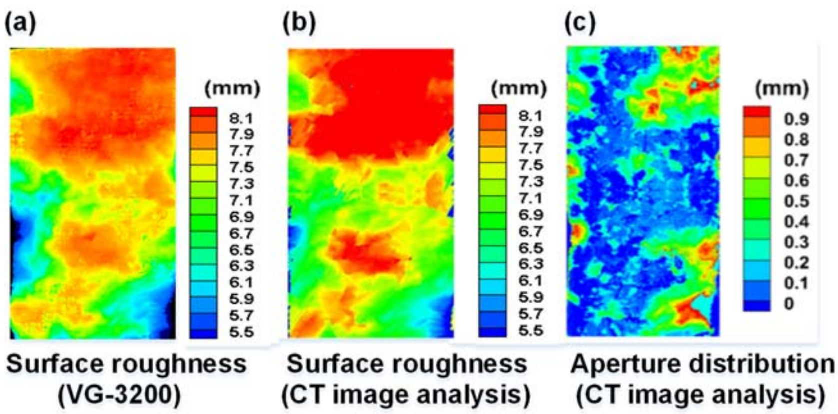

Fig.8 Contour maps of surface roughness (A-Side as mentioned in **Fig.1**) and aperture distribution of Sample #2 at 0 MPa. (a) surface roughness obtained through VG-3200 pattern projection, (b) surface roughness measured through the CT image analysis, and (c) aperture distribution measured through the CT image analysis.

3. Experimental results

3.1 Short-term permeability tests

Figure 9 illustrates the changes in permeability with different levels of confining pressure and temperature. In the figure, the right-pointing and left-pointing triangles represent the loading and unloading processes, respectively. At 20 ºC (**Fig. 9(a)**), the permeability decreases with the increase in confining pressure, and increases with the decrease in confining pressure throughout the tests. In particular, the permeability changes greatly and irreversibly in the first cycle of the loading-to-unloading process. Before the first cycle, the fractures may be ill-mated, and the matedness is improved through the first cycle. In the second and third cycles, reversible hysteresis curves are observed.

At 60 and 90 ºC (**Figs. 9(b)** and **(c)**), the similar changes in permeability that alter with the confining pressure, are observed. Namely, the permeability shows the reversible behavior in the loading-unloading processes. The results indicate that mechanical compaction should exert a significant influence on the permeability. The impact may be greater than the influence of the prescribed temperature. However, the measured permeability also shows a clear temperature-dependence; it decreases with the increase in temperature as shown in **Fig. 9(d)**. In this figure, the third cycle of the permeability variation at each temperature is selected for the comparison. At 90 ºC, the permeability decreases from the order of 10^{-12} to that of 10^{-14} m^2, which is much smaller than that at 20 and 60 ºC. It is inferred that thermal expansion results in the aperture decrease and the fracture contact-area increase. Moreover, other potential factors, such as the pressure solution or geochemical responses, might function against the mechanical deformation and induce irreversible permeability behavior (Polak et al., 2003,2004; Yasuhara et al., 2006,2015).

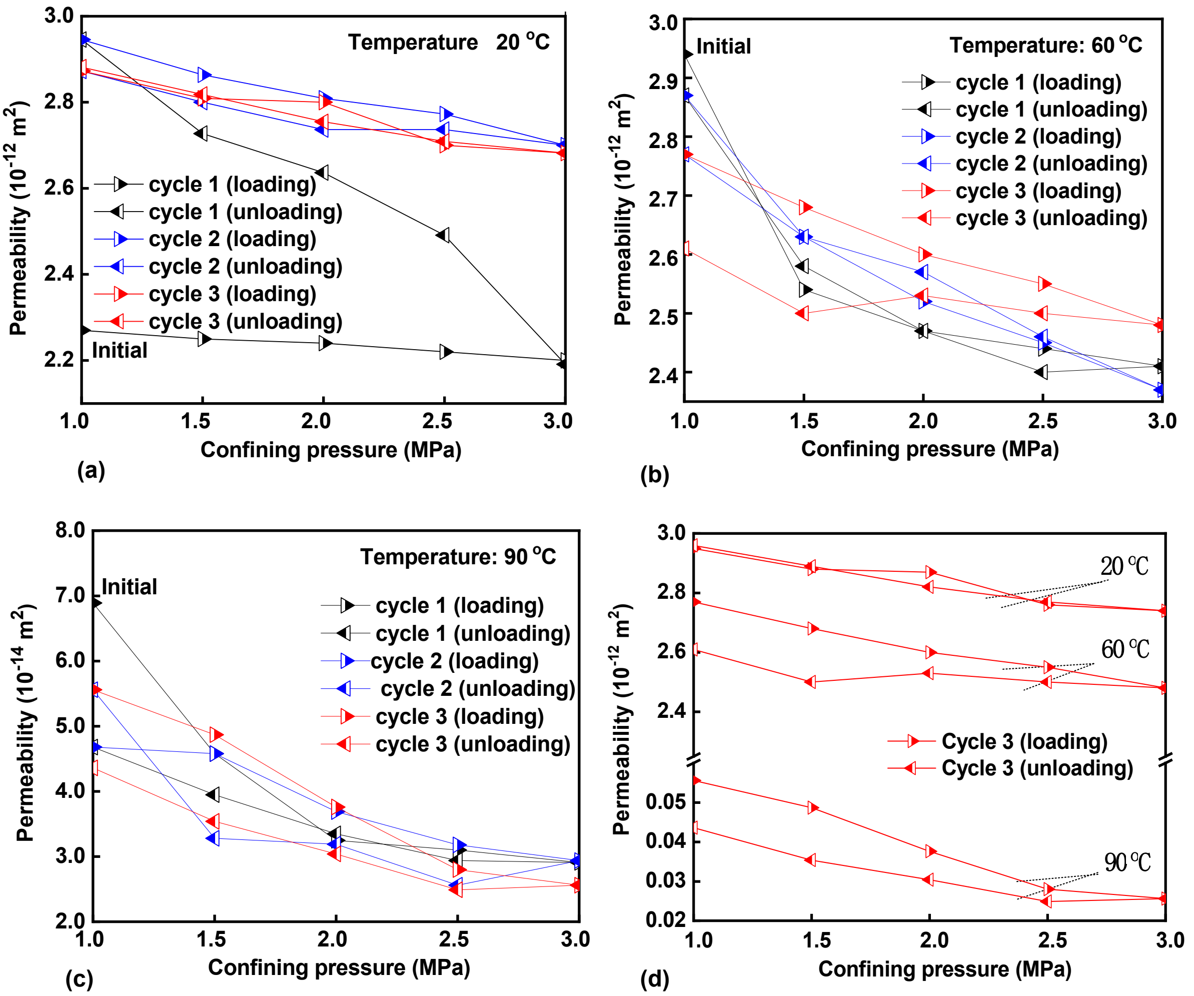

Fig. 9 Short-term test results: (a) permeability variation at 20 ºC, (b) permeability variation at 60 ºC, (c) permeability variation at 90 ºC and (d) permeability variation in third cycle under different temperature conditions

3.2 Long-term permeability tests

Before the commencement of the long-term tests, the permeability increases from 4.36 $\times 10^{-14}$ m^2 to 4.18 $\times 10^{-13}$ m^2 after the temperature is decreased from 90 to 20 ℃ at 1.0 MPa. This change is attributed to the increase in pore volume due to the decrease in temperature.

Figure 10 shows the temporal change in the permeability measured in the long-term tests under the constant confining pressure of 3.0 MPa. The initial permeability is 3.7 $\times 10^{-13}$ m^2. The permeability drops sharply within several days and decreases about 45 % of the initial value. This change can be interpreted as the mechanical compaction changing the permeability.

Subsequently, permeability resumes its decrease after a short stable period. The permeability decreases to 87 % of the initial value between 30 and 120 days. Creep deformation might lead to a reduction in permeability when the fluid passes through a stressed fracture. From 120 to 180 days, the permeability shows a slight increase. At the end of the 180-day test, the permeability value reaches to 7× 10^{-14} m^2.

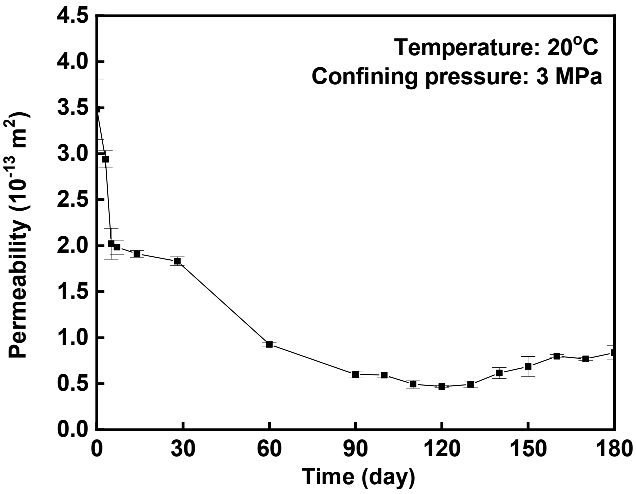

Fig. 10 Change in permeability with time (Sample #1) at 20 ℃,180 days

At the end of the long-term permeability tests, the confining pressure has been unloaded to 1.0 MPa. The permeability evolution during the long-term cycle of the loading-to-unloading process after the 180-day holding is shown in **Fig. 11(a)**. Although the permeability within the unloading process shows a little change, an irreversible reduction in permeability is observed between the onset and the end of the test. This trend is incongruous with the observation made by Yasuhara et al. (2013) (**Fig. 11(b)**), in which the long-term permeability test was conducted under a constant confining pressure of 10.0 MPa, at 20 ºC for 35 days.

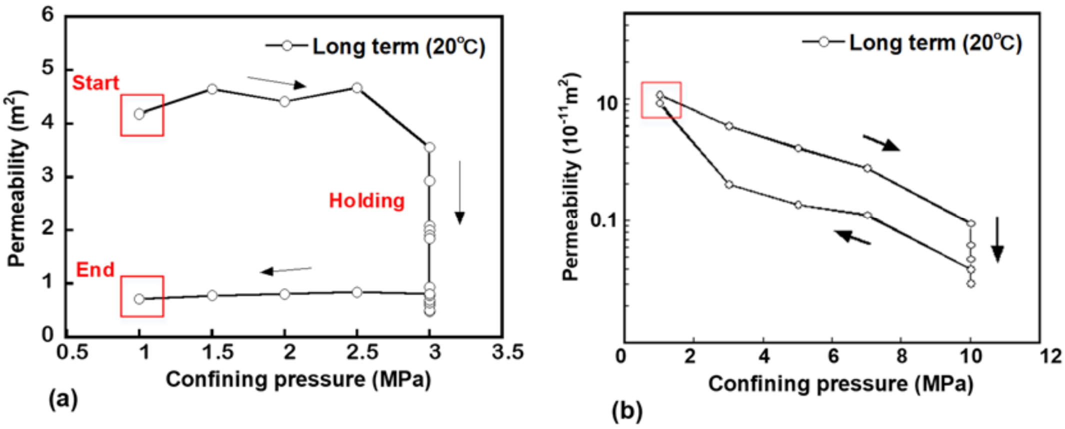

Fig. 11 Comparison of changes in permeability between (a) current work and (b) Yasuhara et al. (2013)

The irreversible permeability change is supposed that the propping asperities of the fracture surfaces are truncated under a relatively long confining condition probably induced by mechanical crushing and/or geochemical reactions such as pressure solution (Yasuhara et al., 2015). To verify the geochemical response within the fracture, the effluent from the internal fracture is checked about the element composition change with the ICP analysis. The element composition and the concentration results are shown in **Fig. 12**. The concentrations of Si, Na and Ca are larger than the others. It can be seen from the results of 0 to 30 days that the concentrations of each element become larger. From 30 to 180 days, those elements show a slight fluctuation. These results verify that the pressure solution may generate under a long-term confining condition, and it may evolve the fracture topography with time.

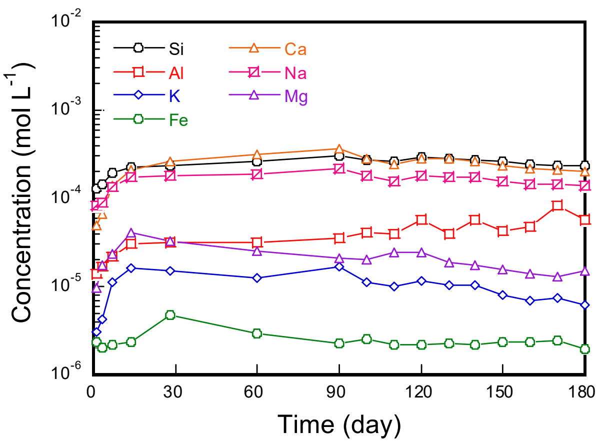

Fig. 12 Evolution of mineral composition in long-term permeability test at 20 °C,180 days

3.3 Observation results using microfocus X-ray CT

3.3.1 Variation in aperture distribution

The irreversible permeability reduction observed in the long-term tests indicates that the fracture aperture distribution will be permanently changed with time. As the important parameters for characterizing the flow paths within the fracture, the geometries of the fracture surfaces and fracture contact-area are investigated by the X-ray CT technique.

Figure 13 shows the temporal change in the aperture distribution evaluated by the CT image analysis. In **Figs.13 (a)** and **(b)**, it is clearly seen from the contour maps that the blue-colored area (i.e., fracture contact-area) increases with the increase of the confining pressure. When closely observing **Figs. 13 (b)** to **(d)**, the blue-colored area seems monotonically increasing with time. Namely, the fracture contact-area is enlarged. In **Fig.13 (e)**, the aperture decrease with time can be clearly observed from the CT images, and it is corresponding to the image analysis results.

Therefore, the fracture contact-area increase can be explained by two processes. In the first process, the fracture aperture is drastically decreased due to the mechanical compaction by the increased confining pressure, which is similar to the permeability behavior observed in the short-term tests. In the second process, the creep deformation induces the long-term alteration of the fracture roughness surface under the constant confining pressure. Obviously, the second process also results in the long-term evolution of the fracture permeability.

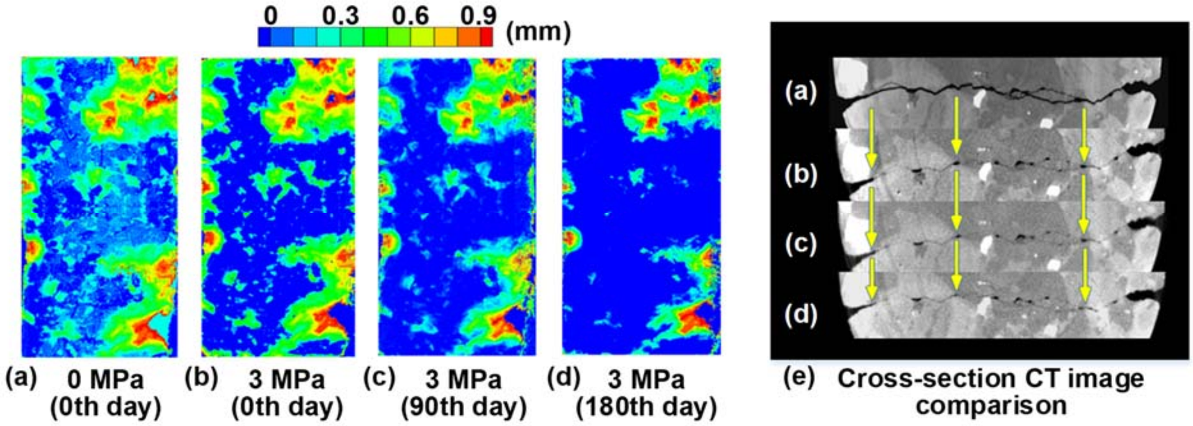

Fig. 13 Temporal changes in aperture variation evaluated from CT analysis in long-term tests: (a) initial value of mean aperture at 0 MPa, (b) aperture variation after 0 days at 3.0 MPa, (c) after 90 days; (d) after 180 days and (e) cross-section CT images comparison from (a) to (d)

3.3.2 Quantification of mechanical aperture and fracture contact-area ratio

Figure 14(a) and **(b)** present temporal changes in the mean values of the mechanical aperture and the fracture contact-area ratio calculated by the image analysis, respectively. The aperture value drastically decreases from 0 MPa to 3.0 MPa and the contact-area ratio increases from 5% to 33%. At a constant confining pressure of 3.0 MPa, the mechanical aperture decreases gradually to 7.5 % from 0 to 90 days. Then, it further decreases to 10 % from 90 to 180 days. Simultaneously, the tendency for the fracture contact-area ratio increasing is confirmed. The contact-area ratio reaches approximately 37 % at 180 days.

Previous studies used numerical methods to evaluate the fracture contact-area ratio. Yasuhara et al. (2004) predicted the fracture contact-area ratio less than 30 % at 2.73 MPa and higher temperatures ranging from 80 to 150 ºC. In contrast, the contact-ratio value evaluated in this study is larger than 30 % at 3.0 MPa - the calculated value tends to be relatively overestimated compared to those predicted values in the previous studies. The possible reasons for the discrepancy may be due to the accuracy of the image analysis method as introduced in section 2.5.2, the spatial resolution of CT images, and so on. It is certain, however, that no previous laboratory study other than the current study has verified the long-term change in the actual contact ratio value with/without confining pressure. Moreover, the tendency for the contact-area ratio increase calculated by the image analysis is in good agreement with the decrease in the fracture aperture observed by the CT scan. In this viewpoint, the experimental observation of the fracture contact-area ratio is one of the variable findings in this study, which successfully captures an actual phenomenon of the rock fracture evolution, i.e., the fracture contact-area increasing under the constant confining pressure.

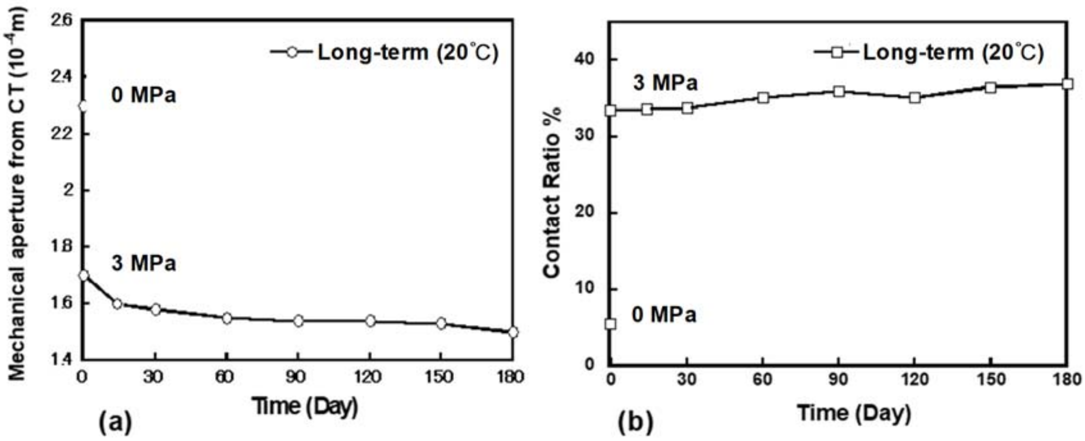

Fig. 14 Temporal changes in (a) mean aperture value and (b) contact-area ratio variation from CT image analysis

4. Discussions

4.1 Short- and long-term permeability tests

Figure 15 shows a summary of the permeability tests, in which red points represent the permeability values at 1.0 MPa, and blue points are the values at 3.0 MPa. It is clearly seen that permeability is sensitive to the confining pressures in the short-term. The permeability value at 1.0 MPa is larger than that at 3.0 MPa. Then the temperature was then reduced to 20 ºC again after the short-term tests. The permeability value seems increase, however, it cannot reach the initial value of the short-term test at 20 ºC. Moreover, the permeability is not sensitive to the confining pressure when reloading the confining pressure again.

At the long-term tests, the permeability decreases remarkably in the early period, which is probably resulted from the mechanical compaction due to an increment of confining pressure (see CT images **Figs. 13(a)** and **(b)**). Permeability value after the long-term test is slightly higher than the value at the short-term 90 °C. It indicates that the internal fracture aperture is deformed with time in the long-term. The irreversible crushing and/or dissolution at the contacting asperities, rather than elastic and reversible compaction, might be a reason for the phenomena in the long-term tests (Yasuhara, et al., 2015).

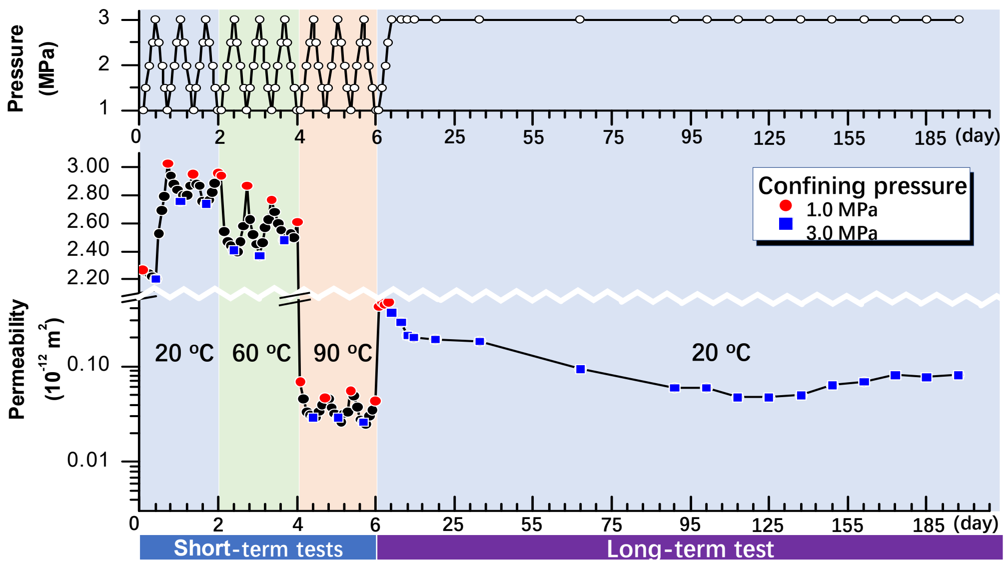

Fig. 15 Summary of permeability changes in short- and long-term tests

4.2 Relation between hydraulic aperture and mechanical aperture

Figure 16(a) shows a comparison of the mechanical aperture measured by the CT observation and the hydraulic aperture which is calculated from the mechanical aperture. The mechanical aperture shows a relationship between the hydraulic aperture and the fracture contact-area ratio, as defined by, Farough et al. (2016).

$$b_H^3 = b_M^3(1-R_C)/(1+R_C) \quad (7)$$

where b_H is the hydraulic aperture, b_M is mechanical aperture measured from CT observation, and R_C is the fracture contact-area ratio calculated from CT image analysis. It is noted from **Fig. 16(a)** that hydraulic aperture is lower than the mechanical aperture, which is congruent with the previous studies that the real roughness characteristics influence the fluid passing through the aperture, and result in the hydraulic aperture lower than the mechanical aperture (Bandis et al., 1985; Renshaw,1995; Zimmerman et al.,2004; Liu, 2005;Kishida et al., 2013).

4.3 Relation between permeability and internal fracture structure

To investigate the correlation between variations in the permeability and the fracture aperture, the relation between hydraulic aperture measured from the permeability tests and that calculated from the X-ray CT observation of the mechanical aperture is discussed. **Figure 16(b)** shows a comparison of the hydraulic apertures. The hydraulic aperture obtained from the permeability test is always lower than that obtained from the X-ray CT. From the initial hydraulic aperture value to the end value after 180 days, the decreasing gradient of the hydraulic aperture obtained from the permeability tests is about 52 % and the decreasing gradient from the CT is about 12 %.

The difference in the decreasing gradient mentioned above will be summarized for two reasons. Firstly, the granite Sample #1 experiences various levels of temperature and confining pressure in the short-term tests before the long-term tests, whereas the granite Sample #2 is used only for the long-term permeability tests. The fracture roughness surfaces of Sample #1 are deformed during the short-term tests under the coupled conditions. This deformation results in the evolution of the aperture and the decrease of the initial aperture value. Secondly, the two samples are different in size, which should also generate the initial aperture difference.

However, from **Fig.16(b)**, it is noted that the hydraulic aperture evolutions obtained by the permeability tests and X-ray CT are quite similar. Both of them show that the hydraulic aperture decreases with time. From this comparison, the reason for the permeability decreasing in the long-term can be explained by the temporal change in the fracture aperture.

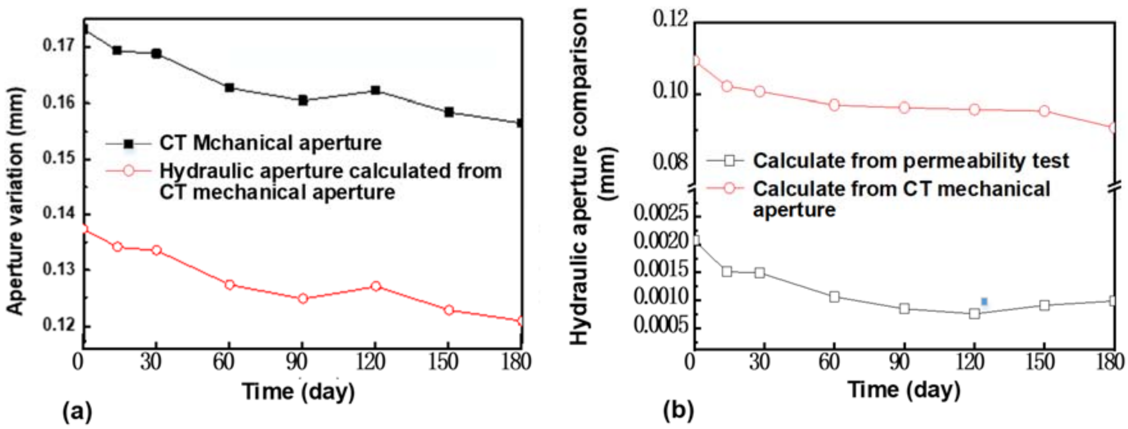

Fig. 16 (a) Comparison result of CT mechanical aperture and hydraulic aperture. (b) Comparison of changes in hydraulic aperture calculated from permeability tests and from CT observation of mechanical apertures

5 **Conclusions**

This study carried out a series of short- and long-term permeability tests under various conditions. To clarify the long-term permeability evolution, variations in the fracture aperture and fracture contact-area were investigated using a microfocus X-ray CT and image analysis technique. The relation between the hydraulic aperture obtained from the permeability tests and that estimated from the X-ray CT observation was evaluated. The influence of the internal fracture structure variation on the permeability was discussed. The conclusions are drawn as follows:

1) In the short-term permeability tests, permeability is sensitive to the confining pressures and temperatures and shows a clear temperature-dependence - it drastically decreases when applying a high temperature of 90 °C. The internal fracture may be reversibly deformed, and permeability is not sensitive to the confining pressure when reloading the confining

pressure again before starting the long-term tests. In the long-term tests, permeability evolution showed that the internal fracture structure was irreversibly deformed under a long-term compaction condition. This deformation will change permeability behavior.

2) Triaxial apparatus coupled with the microfocus X-ray CT equipment was developed in this study, to observe the long-term fracture structure change under various levels of confining pressures and temperatures. Results show that the fracture aperture decreases with increase of the confining pressure from 0 MPa to 3 MPa, and it gradually decreases with time at the constant confining pressure of 3MPa during 180 days.

3) The morphology of the fracture surface roughness was successfully obtained by the CT image analysis, which showed quite similar to that was obtained by the optical profilometer. The fracture contact-area ratios calculated by the image analysis are relatively larger than those shown in the literature. However, this study successfully obtains the contact-area ratio through the experimental approach and captures the long-term evolution of an actual rock fracture structure, i.e., the increase in the fracture contact area with time under the constant confining pressure.

4) The hydraulic aperture value measured from the long-term permeability tests is lower than that estimated from the X-ray CT. This mismatch is probably attributed to the difference of the sample size. Moreover, before the long-term permeability tests, Sample #1 experienced short-term permeability tests, and the aperture distribution has been altered under the coupled conditions, while Sample #2 was not used to conduct any pre-tests. Those reasons may lead to the difference in the hydraulic aperture values.

5) The decreasing gradient of the hydraulic aperture measured from the permeability tests is qualitatively similar to that estimated from the CT observation. Therefore, the fracture

contact-area increase under the constant confining pressure links to the permeability decrease in the long-term.

Acknowledgments

This work was supported by the KAJIMA Foundation, Japan and by the Ministry of Education, Culture, Sports, Science and Technology (MEXT) scholarship (Project Code No. 2015-9056, Certificate No.201508210170), Japan. Their support is gratefully acknowledged.

References

1. Frdric, B., Frank, L., Pierre, D.C., Valr, D., 2017. Implications of safety requirements for the treatment of THMC processes in geological disposal systems for radioactive waste. Journal of Rock Mechanics and Geotechnical Engineering.9(3):428-434. Berniera, F., Lemy, F., De Cannièrea, P., Detilleuxb, V., 2017. Implications of safety requirements for the treatment of THMC processes in geological disposal systems for radioactive waste. *Journal of Rock Mechanics and Geotechnical Engineering*. 9(3):428-434.
2. Ghassemi,_A., Kumar, G.S., 2007. Changes in fracture aperture and fluid pressure due to thermal stress and silica dissolution/precipitation induced by heat extraction from subsurface rocks**.** Geothermics.36:115-140.
3. Taron, J., Elsworth, D., 2010. Coupled mechanical and chemical processes in engineered geothermal reservoirs with dynamic permeability. International Journal of Rock Mechanics and Mining Sciences.47(8):1339-1348.
4. Tsang, C.F., Barnichon, J.D., Birkholzer, J., 2012. Coupled thermo-hydro-mechanical processes in the near field of a high-level radioactive waste repository in clay formations. International Journal of Rock Mechanics and Mining Sciences.49:31-44.
5. Rutqvist, J., Wu, Y.S., Tsang, C.F., 2002. A modeling approach for analysis of coupled multiphase fluid flow, heat transfer,

and deformation in fractured porous rock. International Journal of Rock Mechanics and Mining Sciences.39:429–442.

6. Yasuhara, H., Kinoshita, N., Ohfuji, H., Kishida, K., 2015. Long-term observation of permeability in sedimentary rocks under high-temperature and stress conditions and its interpretation mediated by microstructural investigations. Water Resources Research.51(7):5425-5449.

7. Xu, P., Yang, S.Q., 2016. Permeability evolution of sandstone under short-term and long-term triaxial compression. International Journal of Rock Mechanics and Mining Sciences.85:152-164.

8. Yasuhara, H., Polak, A., Elsworth, D., 2006. Evolution of fracture permeability through fluid-rock reaction under hydrothermal conditions. Erath Planetary Science Letters.244:186–200.

9. Yasuhara, H, Elsworth, D., 2004. Evolution permeability in a natural fracture: significant role of pressure solution. Journal of Geophysical Research.109(B03204):1029-1038.doi:10.1029/2003JB002663.

10. Yasuhara, H., Kinoshita, H., Kishida, K., 2011. Temporal alteration of fracture permeability in granite under hydrothermal conditions and its interpretation by coupled chemo-mechanical model. Applied Geochemistry.26:2074-2088.

11. Polak, A., Elsworth, D., Liu, J., 2004. Spontaneous switching of permeability changes in a limestone fracture with net dissolution. Water Resource. Research.40(W03502).

12. Beeler, N.M., Hickman, S.H., 2004. Stress-induced, time-dependent fracture closure at hydrothermal conditions. Journal of Geophysical Research: Solid Earth.109(B02211).

13. Elkhoury, J.E., Detwiler, R.L., Ameli, P., 2013. Dissolution and deformation in fractured carbonates caused by flow of CO2-rich brine under reservoir conditions. International Journal of Greenhouse Gas Control.16:203-215.

14. Wang, Y., 2017. On subsurface fracture opening and closure. Journal of Petroleum Science and Engineering.155:46-53.

15. Zhang, C., Liu, X., Liu, Q., 2013. A thermo-hydro-mechano-chemical formulation for modeling water transport around a ventilated tunnel in an argillaceous rock. Journal of Rock Mechanics and Geotechnical Engineering.5(2):145-155.

16. Li, B., Jiang, Y.J., Koyama, T., Jing, L.R., Tanabashi, Y., 2008. Experimental study of the hydro-mechanical behavior of rock joints using a parallel-plate model containing contact areas and artificial fractures. International Journal of Rock

Mechanics and Mining Sciences.45(3):362-375.

17. Polak, A,. Elsworth, D., Yasuhara, H., 2003. Permeability reduction of a natural fracture under net dissolution by hydrothermal fluids. Geophysical Research Letters.30(20).

18. Farough, A., Moore, D.E., Lockner, D.A., Lowell, R.P., 2016. Evolution of fracture permeability of ultramafic rocks undergoing serpentinization at hydrothermal conditions: An experimental study. Geochemistry, Geophysics, Geosystems.17(1):44-55.

19. Zimmerman, R.W., Bodvarsson, G.S., 1996. Hydraulic conductivity of rock fractures. Transport in Porous Media.23:1-30.

20. Kishida, K., Sawada, A., Yasuhara, H., 2013. Estimation of fracture flow considering the inhomogeneous structure of single rock fractures. Soils and Foundations.53(1):105-116.

21. Ketcham, R.A., Slottke, D.T., Sharp, J.M., 2010. Three-dimensional measurement of fractures in heterogeneous materials using high-resolution X-ray computed tomography. Geosphere.6:499–514.

22. Van, G. M., Swennen, R., David, P., 2001. Quantitative coal characterisation by means of microfocus X-ray computer tomography, colour image analysis and back-scattered scanning electron microscopy. International Journal of Coal Geology.46:11–25.

23. Yao, Y., Liu, D., Che, Y., 2009. Non-destructive characterization of coal samples from China using microfocus X-ray computed tomography. International Journal of Coal Geology.80:113–23.

24. Fan, H.Z., Jian, C.G., Shou, M., 2018. 3D observations of the hydraulic fracturing process for a model noncemented horizontal well under true triaxial conditions using an X-ray CT imaging technique. Journal of Natural Gas Science and Engineering. 52:128-140.

25. Robert, A.J., John, S.S., Louis, M.C., Paul, V.R., 1993. Nondestructive Measurements of Fracture Aperture in Crystalline Rock Cores Using X Ray Computed Tomography. Journal of Geophysical Research.98(B2):1889-1900.

26. Dustin, C., Johnathan, M.B., Magdalena, G.B., 2017. CT scanning and flow measurements of shale fractures after multiple shearing events. International Journal of Rock Mechanics and Mining Sciences.100:177–187.

27. Lu, X., Ryan, T., Armstrong., 2018. High-pressure X-ray imaging to interpret coal permeability.Fuel.226:573–582.

28. Kumaria, W.G.P., Ranjith, P.G., Pererab, M.S.A., Li, X., 2018. Hydraulic fracturing under high temperature and pressure conditions with micro CT applications: Geothermal energy from hot dry rocks.Fuel.230:138–154.

29. Karpyn, Z.T., Alajmi, B.A., Radaelli, C.F., 2009. X-ray CT and hydraulic evidence for a relationship between fracture conductivity and adjacent matrix porosity. Engineering Geology.103:139–145.

30. Stephanie, P., Bertels., David, A., 2001. Measurement of aperture distribution, capillary pressure relative permeability, and in situ saturation in a rock fracture using computed tomography scanning.Water Resource Research.37(3):649-662.

31. Karpyn, Z.T., Grader, A.S., Halleck, P.M., 2007. Visualization of fluid occupancy in a rough fracture using micro-tomography. Journal of Colloid and Interface Science.307:181–187.

32. Mazumder, S., Wolf, K., Elewaut, K., Ephraim, R., 2006. Application of X-ray computed tomography for analyzing cleat spacing and cleat aperture in coal samples. International Journal of Coal Geology.68:205–22.

33. Keller, A., 1998. High resolution, non-destructive measurement and characterization of fracture apertures. International Journal of Rock Mechanics and Mining Sciences.35:1037-1050.

34. Hamed, L.R., Ryan, T., Armstrong, P.M., 2016. Micro-CT image calibration to improve fracture aperture measurement. Case Studies in Nondestructive Testing and Evaluation.6:4–13.

35. Yao, Y.B., Liu, D.M., Che, Y., 2009. Non-destructive characterization of coal samples from China using microfocus X-ray computed tomography. International Journal of Coal Geology.80:113–123.

36. Richard, A., Ketcham, Donald, T., 2010. Three-dimensional measurement of fractures in heterogeneous materials using high-resolution X-ray computed tomography.Geosphere.6(5):499–514.

37. Kawakata, H., Cho, B.T., Kiyama, C.T., 1999. Three-dimensional observations of faulting process in Westerly granite

under uniaxial and triaxial conditions by X-ray CT scan. Tectonophysics.313:293–305.

38. Okamoto, A., Tanaka, H., Watanabe, N., Saishu, H., Tsuchiya, N., 2017. Fluid Pocket Generation in Response to Heterogeneous Reactivity of a Rock Fracture Under Hydrothermal Conditions. Geophysical Research Letters.44(20):10306-10315.

39. Kamali-Asl, A., Kc, B., Foroutan, M., Ghazanfari, E., Cladouhos, T., 2018. Experimental study of fracture response in granite specimens subjected to hydrothermal conditions relevant for enhanced geothermal systems.Geothermics.72:205-224.

40. Caulk, R.A., Ghazanfari, E., Perdrial, J.N., Perdrial, N., 2016. Experimental investigation of fracture aperture and permeability change within Enhanced Geothermal Systems. Geothermics.62:12-21.

41. Fairhurst, C., 1964. On the validity of the ‘Brazilian’ test for brittle materials. International Journal of Rock Mechanics and Mining Sciences.1(4):535–546.

42. Barton, N., Quadros, D.E.F., 1997. Joint aperture and roughness in the prediction of flow and groutability of rock masses. International Journal of Rock Mechanics and Mining Sciences.34:3-4.

43. Barton, N., Choubey, V., 1977. The Shear Strength of Rock Joints in Theory and Practice. Rock Mechanics. 10: 1-65. 1977.

44. Tse, R., Cruden, D.M., 1979. Estimating joint roughness coefficients, International Journal of Rock Mechanics and Mining Sciences.16:303-307.

45. Zhang, G.C., Karaku, S.M., Tang, H.M., 2014. A new method estimating the 2D Joint Roughness Coefficient for discontinuity surfaces in rock masses. International Journal of Rock Mechanics and Mining Sciences.72:191-198.

46. Dimadis, G., Dimadi, A., Bacasis, I., 2014. Influence of fracture roughness on aperture fracture surface and in fluid flow on oarse-grained marble, experimental results. Journal of Geoscience and Environment Protection.2:59-67.

47. Yong , R., Ye, J., Liang, Q.F., 2018. Estimation of the joint roughness coefficient (JRC) of rock joints by vector similarity measures. Bull Eng Geol Environment.

48. Yin, Q., Ma,G.W., Jing, H.W., 2017. Hydraulic properties of 3D rough-walled fractures during shearing: An experimental study. Journal of Hydrology.555:169-184.

49. Hsieh, P. A., Tracy, J.V., Neuzil, C.E., 1981. A transient laboratory method for determining the hydraulic properties of ‘tight’ rocks—I. Theory. International Journal of Rock Mechanics and Mining Sciences & Geomechanics Abstracts.18:245-252.

50. Otani, J., Mukunoki, T., and Obara, Y. 2002. Characterization of failure in sand under triaxial compression using industrial X-ray CT scanner. International journal of physical modeling in geotechnics.2:15-22.

51. Kido, R., Higo,Y., Takamura, F., Morishita, R., Khaddour, G., 2020. Simon Salager Morphological transitions for pore water and pore air during drying and wetting processes in partially saturated sand, Acta Geotechnica.

52. Rosenfeld ,A., Kak, A.C., 1982. Digital Picture Processing, San Diego, CA: Academic Press.

53. Higo, Y., Oka, F., Morishita, R., ,Matsushima, Y., Yoshida, T., 2014. Trinarization of μX-ray CT images of partially saturated sand at different water-retention states using a region growing method. Nuclear Instruments and Methods in Physics Research Section B: Beam Interactions with Materials and Atoms.324:63-69.

54. Otsu, N., 1979. A Threshold Selection Method from Gray-Level Histogram. IEEE Trans. Systems Man, and Cybernetics.9:62-66.

55. Yasuhara , H., Hasegawa, D., Nakashima, S., Kishida, K., 2013. Experimental evaluation of fracture permeability in granite under temperature and stress controlled conditions. Japanese Geotechnical-Journal.8:71-79.

56. Walsh, J.B., 1981. The Effect of Pore Pressure and Confining Pressure on Fracture Permeability. International Journal of Rock Mechanics and Mining Sciences.18:429-435.

57. Bandis, S., Makurat, A., Vik, G., 1985. Predicted and measured hydraulic conductivity of rock joints. International Symposium. Fundamentals of Rock Joints, Bjørkliden.269–280.

58. Renshaw, C.E., 1995. On the relationship between mechanical and hydraulic apertures in rough-walled fractures. Journal of Geophysical Research: Solid Earth.100(B12):24629-24636.

59. Liu, E., 2005. Effects of fracture aperture and roughness on hydraulic and mechanical properties of rocks: implication of seismic characterization of fractured reservoirs. Journal of Geophysics and Engineering.2(1):38-47.

60. Zimmerman, R.W., Main, I.G., 2004. Chapter7-Hydromechanical behaviour of fractured rocks. International Geophysics.89:361–419.